




Electro-discharge sintering of nanocrystalline NdFeB magnets: process parameters, microstructure, and the resulting magnetic properties

Lennart Leich^{1,*} , Arne Röttger¹, Rene Kuchenbecker¹, and Werner Theisen¹

¹Institut für Werkstoffe, Lehrstuhl Werkstofftechnik, Ruhr Universität Bochum, Universitätsstraße 150, 44801 Bochum, Germany

Received: 15 June 2020

Accepted: 28 September 2020

Published online:

12 October 2020

© The Author(s) 2020

ABSTRACT

This study investigates the compaction of nanocrystalline NdFeB magnet powder by electro-discharge sintering (EDS). On this account, process parameters, microstructure, and the associated magnetic properties of the EDS-densified nanocrystalline NdFeB specimens were investigated by varying the discharge energy E_{EDS} and compression load p_{EDS} . Although optimized process parameters could be evaluated, three different microstructures (fully densified zone, insufficiently densified zone, and melted zone) are present in the EDS-compacted specimens. Thereby, volume fractions of these formed three different microstructures determine the resulting mechanical and magnetic properties of the specimens. For all specimens, the intrinsic coercivity H_{cJ} deteriorates with increasing discharge energy, as the generated Joule heat leads to microstructural changes (grain growth, dissolution of magnetic phases), which reduces the magnetic properties. The compression load has less influence on the coercivity H_{cJ} , as it only affects the initial resistance of the pre-compacted powder loose. The residual induction B_r deteriorates with increasing the discharge energy due to microstructural changes. An increase in the compression load p_{EDS} results in an increase in the specimens' density and thus promotes the residual induction B_r .

1 Introduction

As an enabler and driver of technology, permanent magnets have gained increasing importance over the last half-century and they are a critical part of many high-tech products, such as electric vehicles, electric generators of wind turbines, and consumer

electronics [1]. High-performance rare-earth-based permanent magnets such as NdFeB are indispensable in the miniaturization of electrical devices, the development of highly efficient electric motors, and energy conversion in general [2]. The energy product $(BH)_{max}$ of NdFeB, which is the most important quantity for permanent magnets as it describes the

Address correspondence to E-mail: lennart.leich@rub.de

energy stored in the magnet, is the highest among all permanent magnets in the case of NdFeB magnets. It is theoretically above 500 kJ/m^3 and thus exceeds other permanent magnets at room temperature, which can be attributed to the hard magnetic phase $\text{Nd}_2\text{Fe}_{14}\text{B}$ [3]. Due to the increasing electrification (electromobility, energy storage) it can be assumed that the need for NdFeB magnets will increase in the future. On this account, the research and development of new alloying concepts or more efficient manufacturing processes in the field of NdFeB magnets are still in the focus of researchers [4, 5]. NdFeB permanent magnets can roughly be classified into two categories, the metallic and the bonded magnets. Mostly, fully metallic NdFeB permanent magnets are densified by sintering of microcrystalline powders, which contain an excess of rare earth elements (REE). The REEs build a boundary phase that surrounds the microcrystalline $\text{Nd}_2\text{Fe}_{14}\text{B}$ grains and isolates them from each other, which led to superior magnetic properties [6]. Another possibility to manufacture high-performance NdFeB magnets is to densify plate-shaped powders with a nanocrystalline microstructure, which were produced by melt spinning [3]. The densification of nanocrystalline NdFeB powders cannot be done by a conventional sintering process as the long holding time and high temperature would lead to strong grain coarsening, which is associated with a reduction in the magnetic properties. For the densification of nanocrystalline NdFeB magnets, hot pressing and subsequent hot extrusion have proven to be the best method up to now, since the densification can take place at a lower temperature and in a shorter time due to the pressure support [1]. ECAS (electric current activated/assisted sintering) techniques are short-term sintering techniques and are therefore suitable for the densification of powders, where microstructural changes such as grain coarsening, precipitation, and dissolution reactions should not occur such as nanocrystalline NdFeB powders. The short process time (a few milliseconds up to a few minutes) and fast heating and cooling rates of ECAS techniques should be emphasized. From an economic point of view, the ECAS techniques and especially the EDS process is promising, because the total energy consumption of the EDS process in comparison to conventional sintering techniques is very low. On the one hand, the current heats the metal powder directly (Joule heat) and on the other hand, the compaction process is very fast (5 ms)

[7, 8]. Today more than 50 different principles of ECAS techniques are described in patents and literature [9]. The most popular technique is Spark Plasma Sintering (SPS) [10, 11], but there are several less popular techniques such as electro-discharge sintering (EDS) [12, 13], Resistance Sintering (RS) [14, 15] or Flash Sintering (FS) [16, 17]. Based on a preliminary investigation [18, 19], dense NdFeB magnets could be produced using EDS. Thereby, differently, microstructures could be registered locally in the EDS-densified sample, which in total influence the bulk properties of the EDS-compressed NdFeB magnet. In order to further optimize the properties of EDS-compressed NdFeB magnets, precise knowledge of the locally formed microstructure, and the properties associated with it is essential. This knowledge gap needs to be closed in this work to derive further optimization measures concerning process technology and process parameters.

2 Experimental

2.1 Materials

In this study, commercial melt-spun NdFeB powder from Magnequench was used. The powder has the typical ribbon morphology and a nanocrystalline microstructure, as depicted in Fig. 1a and b. The powder has an average thickness of about $30 \mu\text{m}$ and an average length and width of a few up to a few mm.

The chemical composition of the initial powder is shown in Table 1. According to the manufacturer's specifications, the initial powder has a remanence of 0.78 T and a coercivity of $\geq 1650 \text{ kAm}^{-1}$. The main alloy elements Nd, Fe, and B led to the formation of the hard magnetic phase $\text{Nd}_2\text{Fe}_{14}\text{B}$, whereas Cobalt substitutes Iron and was alloyed to increase the Curie temperature without decrease the remanence or coercivity significantly. As the powder is usually used to process hot-deformed NdFeB magnets, it contains Gallium to improve the workability during hot deforming and simultaneously it increases the coercivity by changing the properties of the intergranular phase.

Fig. 1 **a** Overview of the morphology of the powder particles and **b** Nanocrystalline microstructure of the NdFeB powder

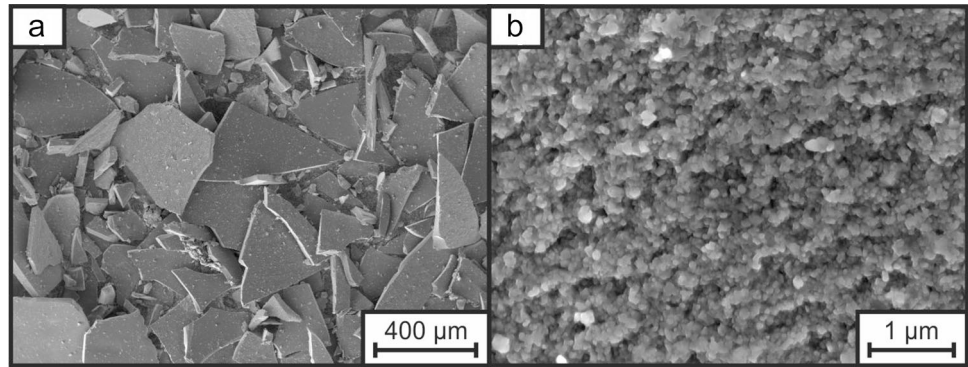


Table 1 Chemical composition in wt% of the nanocrystalline NdFeB powder (manufacturer’s specification)

Element	Nd	Co	B	Ga	Pr	C	Dy	Fe
	30.22	6.02	0.88	0.53	0.20	0.02	0.02	Bal.

2.2 EDS process

A schematic figure of the EDS process as well as a picture of the EDS machine is shown in *Fehler! Verweisquelle konnte nicht gefunden werden..* For all EDS densifications, 10 g of nanocrystalline NdFeB powder (MQU-F) was filled into a cylindrical Si₃N₄ ceramic die with a diameter of 19 mm. The powder loose was then uniaxially pre-compacted with two CuCoBe punches. In this work, the discharge energy E_{EDS} was varied between 40, 48, 56, 64, and 72 kJ. The compression load p_{EDS} was varied among 50, 70, 90, and 110 kN and results in contact pressures of 176 MPa, 247 MPa, 317 MPa, and 388 MPa for a punch diameter of 19 mm. Depending on the degree of densification, the cylindrical specimens have a height between 5.5 and 6.0 mm (Fig. 2).

The measured EDS parameters (compression path, compression load, and the voltage), as well as the calculated resistance (Ohm’s law) of an EDS-densified NdFeB magnet using EDS of 72 kJ and pEDS of 110 kN, are shown in Fig. 3. The shape of the current and voltage curve as a function of time is typical for capacitor discharge. For the used EDS machine current and voltage drops by reaching a time 2 ms after discharge with a maximum of about 170 kA and 12 V. The calculated electrical resistance of the powder loose was taken for a fixed time value. The curve of the compression load decreases during the capacitor discharge, as the generated melt is pressed into the cavities. The curve of the compaction path shows a sinusoidal behavior because the copper plate on which the distance measuring device is placed oscillates after the capacitor discharge. As the period of the sinus is constant, the compression path was taken for a fixed time value.

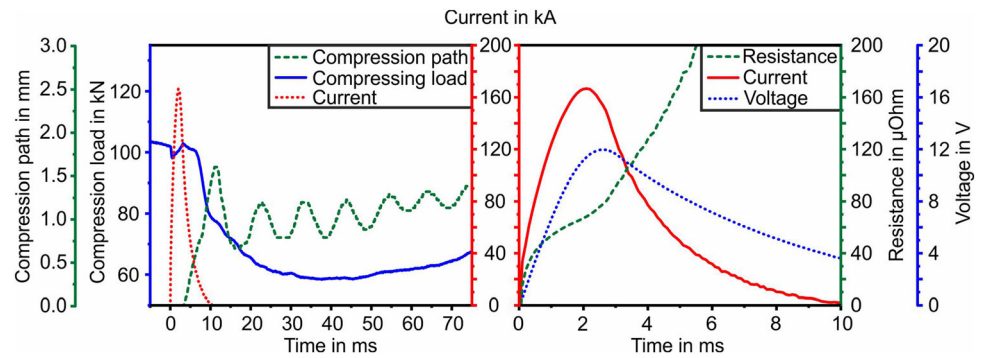
2.3 Material characterization

Microstructural examinations were performed on the one hand with a scanning electron microscope (SEM) of the type TESCAN Mira 3 in the secondary electron



Fig. 2 **a** Schematic diagram of the principle of the EDS process and **b** the EDS machine of the Ruhr-University Bochum and **c** EDS-densified NdFeB magnet (diameter $d = 19$ mm)

Fig. 3 The EDS parameters as a function of time of an EDS-densified NdFeB magnet $E_{EDS} = 72$ kJ and $p_{EDS} = 110$ kN



(SE) and backscattered electron (BSE) modes, a working distance of 8–15 mm, and an acceleration voltage of 15 to 20 kV. Before the microstructural examinations, the specimens were mechanically cut, ground on 18 μm abrasive paper, and polished stepwise with water-free, 3 μm , and 1 μm diamond suspensions. On the other hand, micrographs were made with a transmission electron microscope (TEM) of the type FEI Tecnai F20 G². The acceleration voltage was 200 kV. The images were taken in bright field and STEM dark field mode. High-resolution micrographs were performed in bright field mode. The production of electron transparent lamellas was carried out with a FIB of the type FEI Quanta 200 3D. Phase analysis was performed with a Bruker D8 Discovery X-ray diffractometer using copper K_{α} radiation and a VANTEC-500 area detector with a detector position of 150 mm and a 500 mm collimator. A scanning angle of $2\theta = 25^{\circ}$ – 85° with increments of 10° and a dwell time of 1000 s were used. Diffractograms were evaluated with the program Diffrac.eva using the crystallographic open database (COD). The specimen's density was measured by the Archimedes' principle. The magnetic properties of small specimens were measured using a Physical Property Measurement System (PPMS, Quantum Design) complemented with a vibrating sample magnetometer (VSM). The image analysis was performed with ImageJ. For this purpose, SEM panoramic images from 120 single pictures of the different specimens were taken, the areas of the different microstructures (fully densified, insufficiently densified, and melted) were marked and finally, the different areas were calculated. The magnetic properties of the whole specimens were evaluated with a permagraph system (C-300 from Dr. Steingroever GmbH) after the previous magnetization in a pulsed field.

3 Results and discussion

3.1 EDS process

The influence of the EDS parameters, namely the discharge energy E_{EDS} and the pressing force p_{EDS} , on the discharge current, the calculated resistance, the compression path, and the discharge voltage is depicted in Fig. 4. No temperature measurement is possible during the EDS process because of the fast compaction process, the restricted accessibility for measuring systems, and the inertia of non-optical measuring devices. The discharge current increases for both increasing discharge energies and pressing forces. Using higher discharge energies increases the amount of energy, which is discharged through the sample cross at the same time and thus higher currents are discharged. Higher compression loads lead to an increase of the contact point density and breaking up of oxide layers, thus resulting in lower resistances and according to Ohm's law in higher currents. The compression path decreases if higher compression loads are used as the degree of pre-densification before the discharge is higher.

Using higher discharge energies and higher compression loads leads to decreasing resistances as it's inversely proportional to the current. As mentioned above, higher compression loads lead to an increase of the contact point density and breaking up of oxide layers, thus resulting in lower resistances of the powder loose. Table 2 shows the calculated electrical energy according to formula $E = \int_{t1}^{t2} U * I * dt$ in the secondary circuit (after the transformers) and the percentage of energy relative to the energy of the charged capacitors according to formula $E = \frac{1}{2} * C * U^2$. The measured electric energy in the secondary circuit strongly depends on the applied current and ranges from 20.84 kJ (50 kN / 40 kJ) to

Fig. 4 Measured current, compression path, resistance, and voltage of the EDS-densified NdFeB specimens as a function of the two main process parameters (discharge energy and compression load)

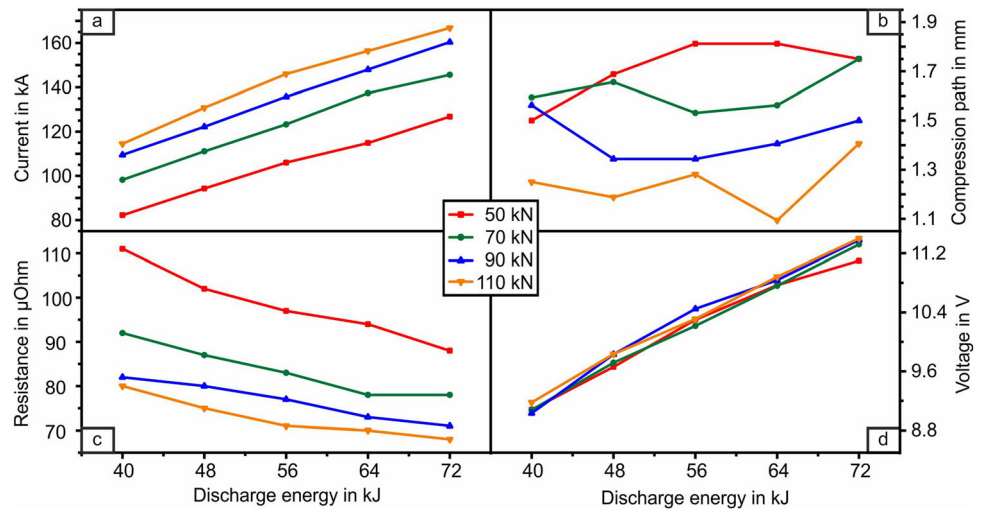


Table 2 Measured electric energy in kJ in the secondary circuit and the efficiency in % with varying discharge energy E_{EDS} and compression load p_{EDS} using 10 g of powder MQU-F

	40 kJ	48 kJ	56 kJ	64 kJ	72 kJ	
50 kN	20.84	25.21	29.62	33.23	38.27	Measured
	51.10	52.52	52.89	51.92	53.15	Efficiency
70 kN	26.74	32.15	37.46	43.66	47.58	Measured
	66.85	66.98	66.89	68.22	66.08	Efficiency
90 kN	30.93	36.53	42.50	48.19	54.19	Measured
	77.33	76.10	75.89	75.30	75.26	Efficiency
110 kN	33.19	40.25	47.46	52.26	57.30	Measured
	83.30	83.85	84.75	81.65	79.58	Efficiency

Table 3 Density ρ in g/cm^3 with varying discharge energy E_{EDS} and compression load p_{EDS} using 10 g of powder MQU-F

	40 kJ	48 kJ	56 kJ	64 kJ	72 kJ
50 kN	6.99	7.02	7.15	7.29	7.42
70 kN	7.25	7.36	7.44	7.55	7.53
90 kN	7.45	7.52	7.55	7.58	7.57
110 kN	7.46	7.51	7.55	7.55	7.56

57.30 kJ (110 kN / 72 kJ). As the resistance of the pre-compacted powder loose is higher for specimens that were densified with lower compression loads, the measured energy is lower. Also, the proportion of generated Joule heat of the total energy (capacitor charge) is higher for the specimens that were densified with lower compression loads, and thus, the measured energy is lower. The microstructural examinations in the next chapter will confirm this assumption.

The impact of the main process parameters, namely compression load p_{EDS} and discharge energy E_{EDS} , on the density of the sample ρ is listed in Table 3. The sample density increases with increasing compression loads and discharge energies. An increase of the compression load leads to an enhancement of the degree of pre-compaction of the loose powder and therefore the specimens possess higher densities after the discharge. Higher discharge

energies led to the formation of a more liquid phase, which also improves the degree of densification. Higher discharge energies cause more Joule heat to be generated, thus increasing the amount of liquid phase and leads to higher densities. Besides, higher compression loads are supporting the movement of the formed liquid phase into the cavities, thus additionally improves the densification during EDS processing.

3.2 Microstructure

Figure 5 shows the microstructure of the EDS-densified NdFeB specimens. Independent of the used EDS process parameters (discharge energy and compression load), three different microstructural zones can be identified in the cylindrically shaped specimens, which in the following are designated as a) fully densified, b) insufficiently densified, and c) melted zones. The local formation of the three different microstructures is schematically illustrated in Fig. 5. These three different zones occur due to the inhomogeneous current distribution inside the specimen, which leads to a temperature gradient during

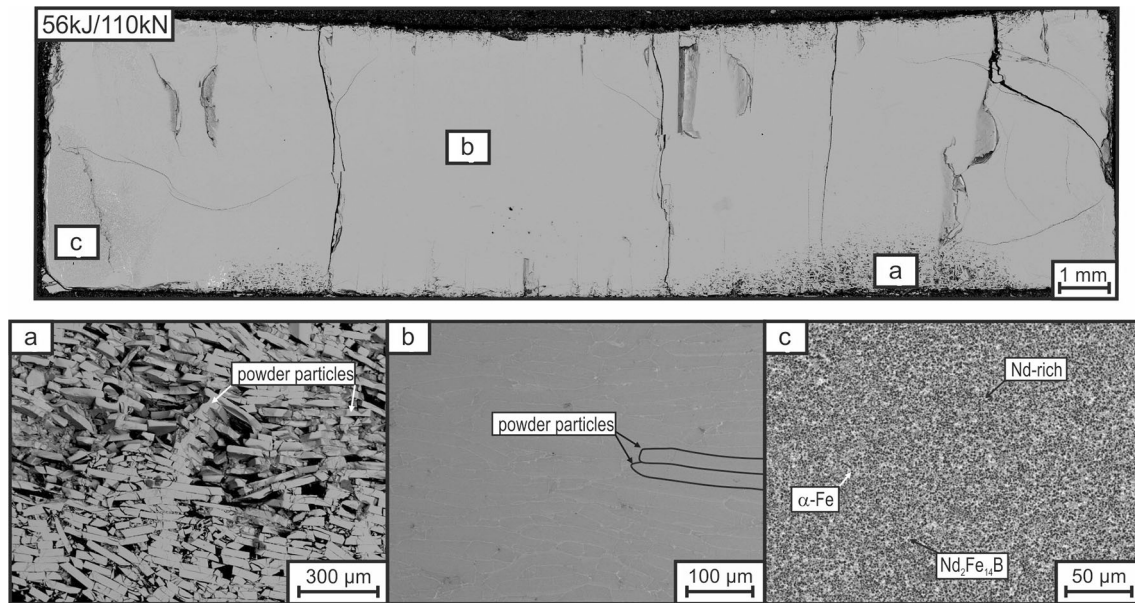


Fig. 5 Above: EDS-densified NdFeB specimen. Below: Three different microstructures in EDS-compacted NdFeB specimens: **a** insufficiently densified zones, **b** fully densified zones and **c** melted zones

discharging. The inhomogeneous temperature distribution is caused by different initial transition resistances inside the pre-compacted loose powder due to uniaxial pressing, which causes local differences in Joule heating.

Additionally, the specimens show cracks. There are various possible reasons for crack formation. Crack formation and propagation may occur during sample preparation (cutting, grinding, polishing) of the brittle material or high-temperature gradients are acting during EDS compaction which can cause the formation of thermal stresses. Also, cracks can occur during the removal of the EDS-compacted samples by the movement of the punch and the die and the consequent introduction of mechanical stresses.

Figure 5b shows the fully densified area, which is the predominant microstructure. The fully densified zone is characterized by powder particles surrounded by a bright phase. This bright phase is formed at the respective particle contact points (high transition resistance) during EDS densification due to Joule heating and dissociation of the phase $\text{Nd}_2\text{Fe}_{14}\text{B}$. The high temperature, which is generated at the respective particle points, promotes the welding of the particles with each other by the formation of a liquid phase in between. Due to the applied compressive load, the liquid and after solidification bright phase can penetrate gaps and therefore promotes the formation of a dense microstructure.

Otherwise, this bright phase is the oxide rich surface of the former powder particles, as NdFeB powder is affine to oxygen, thus forming mainly Nd-rich oxides if the powder is exposed to air.

The insufficient densified zone occurs predominantly in the bottom part of the specimen, as shown in Fig. 5a, dependent on the used process parameters. The insufficient densified zone has a porous structure, and the still visible plate-shaped powder particles are only fused locally together. Increasing the compaction load p_{EDS} and the discharge energy E_{EDS} reduces the volume fraction of the insufficiently densified zone, as shown in Table 4. The lowest compression load and discharge energy lead to an area fraction of 50.45%. If only the compression load is increased, the insufficient densified area can be decreased to 21.56%, while increasing the discharge energy the insufficient densified area can be reduced to 3.75%. If both process parameters are increased to the maximum value, the area fraction can be lowered to a value of 1.65%. High discharge energies promote the formation of the liquid phase in the whole sample and thus increase the degree of densification. High compression loads also reduce the amount of the insufficiently densified zone, which can be attributed to a higher degree of pre-compaction. The used EDS machine is equipped with a uniaxial press, which led to a more inhomogeneous degree of compaction compared to biaxial compressing techniques, which

Table 4 Area fraction of the melted, the insufficient densified, and the fully densified zone in dependence of the used compression load p_{EDS} in kN and the discharge energy E_{EDS} in kJ

	40 kJ	56 kJ	72 kJ
50 kN			
Melted	0.49%	4.85%	16.78%
Insufficient densified	50.45%	13.93%	3.75%
Fully densified	49.06%	81.29%	79.47%
70 kN			
Melted	1.38%	4.14%	19.74%
Insufficient densified	37.41%	11.51%	4.20%
Fully densified	61.21%	84.36%	76.06%
90 kN			
Melted	0.11%	4.36%	11.50%
Insufficient densified	28.87%	5.04%	1.63%
Fully densified	71.02%	90.60%	86.88%
Melted	0.12%	5.03%	9.26%
110 kN			
Insufficient densified	21.56%	5.37%	1.65%
Fully densified	78.32%	89.60%	89.09%

The area fraction was determined using image analysis using the software ImageJ

influences the current distribution. Why the reduction of the insufficient densified area by increasing the compression load is better in contrast to the discharge energy, will be discussed in the following chapter.

The third formed microstructure, namely the melted zone, in the EDS-compacted specimens is characterized by strong segregation, as shown in Fig. 5c. This microstructure is formed due to melting followed by a fast solidification. The amount of melted zone is mainly affected by the discharge energy, whereby higher discharge energies in general increase the amount of the melted zone due to the formation of a high volume fraction of liquid phase during EDS processing. For example, at a constant compression load of 110 kN, the area fraction of the melted zone is increased from 0.12% (40 kJ of discharge energy) to 9.26% (72 kJ of discharge energy). However, the pressing force influences the quantity of the melted zone as well since the pressing force influences the initial resistance and therefore affects the generated Joule heat during energy discharge. At constant discharge energy of 72 kJ, the fraction of the melted microstructure area is decreased with an increasing compression load, as shown in Table 4. Due to the applied load by uniaxial compression, the lower

peripheral areas possess lower densities [20]. This lower degree of compaction influences the current flow as the density of the loose powder is associated with a higher transition resistance between two adjacent particles. This leads to higher heat insertion because of Joule heating, thus promoting the formation of a liquid phase, which is pressed into this lower pre-densified zone. During discharge because of the applied stamp press force. The measured parameters (resistance, energy, current) from the previous section confirm that the specimens densified with lower compression loads have a higher electrical resistances in the pre-compacted powder loose, lower current flows and the measured energies are lower and therefore the proportion of Joule heat was higher. Three different phases are formed, see Fig. 5c, which are black, gray, and brightly colored. As the micrographs were taken using the backscattered electron detector, the black-colored phase is poor in heavy elements, e.g., Nd, and therefore rich in Fe. The brighter phases (gray and bright) are rich in heavy elements such as Nd. As the temperature gradient inside a specimen is inhomogeneous due to the nature of the EDS process, different solidification morphologies occur within the melted zone, as shown in Fig. 6. Related to the work of Gao et al., who described phase formation in undercooled NdFeB alloy droplets [21–23], these three phases are α -Fe (dark), $Nd_2Fe_{14}B$ (gray) and Nd-rich phases.

XRD patterns of the fully densified zones, using both high and low discharge energies, and the melted zone using a diffractometer setting using a collimator to analyze local areas are shown in Fig. 7. These diffractograms confirm the presence of the phases α -Fe and $Nd_2Fe_{14}B$ in the melted zone. At 2θ angles of 28° and 40° , some unidentified diffraction reflections in the diffractogram of the melted zone can be seen and are probably Nd-rich phases. The intensity of the reflections inside the pattern of the fully densified zone decrease with increasing discharge energy, which can be an indication of grain coarsening or a reduction of the number of grains due to a dissociation of the nanocrystalline $Nd_2Fe_{14}B$ phase into α -Fe and Nd-rich phases below the melting temperature, which will be discussed later.

Besides the segregated microstructure, another solidification morphology occurs, see Fig. 6a. It is reasonable to assume that this solidification morphology consists of primary solidified $Nd_2Fe_{17}B_y$ dendrites because of their unique morphology,

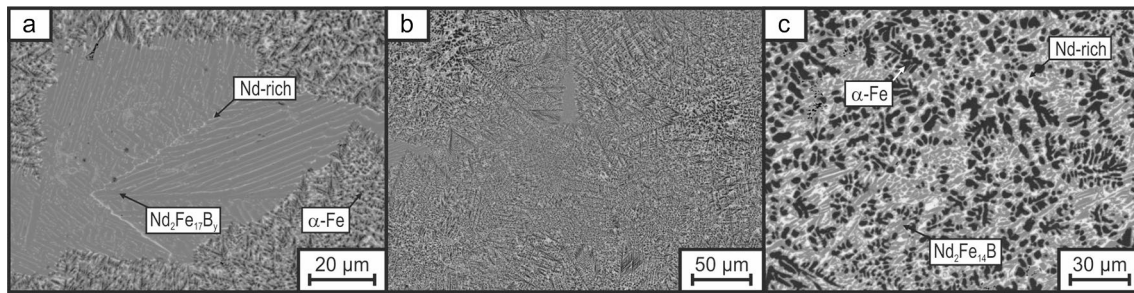
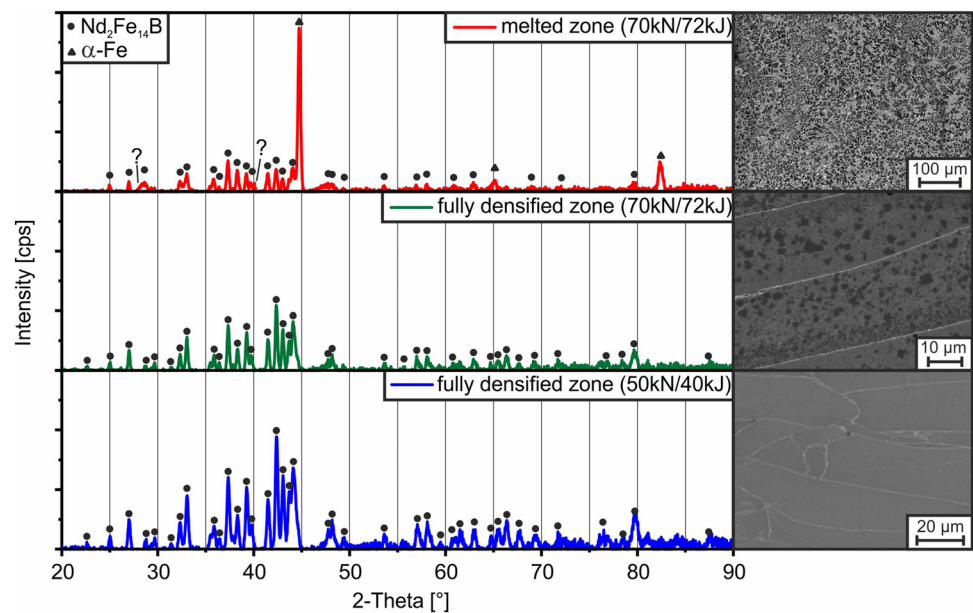


Fig. 6 Different solidification morphologies inside the melted zone of the EDS-densified NdFeB specimen: **a** small area of dendritic $\text{Nd}_2\text{Fe}_{17}\text{B}_y$ and Nd-rich phases; **b** mixed microstructure

with fine and coarse dendritic $\alpha\text{-Fe}$; **c** dendritic $\alpha\text{-Fe}$, interdendritic $\text{Nd}_2\text{Fe}_{14}\text{B}$, and Nd-rich phases

Fig. 7 Diffractograms of the fully densified zones and melted zone



namely a helical appearance with underdeveloped secondary arms [21]. Schneider et al. detected the metastable $\text{Nd}_2\text{Fe}_{17}\text{B}_y$ phase ($y \approx 1$) at high temperatures [24]. During the EDS process, this metastable phase could solidify as the temperature distribution covers a wide temperature range, and due to the fast cooling rates. Between the fully densified zone and the melted zone, a transition zone occurs, see Fig. 8. The transition from the fully compacted zone to the melted zone is characterized by a transition zone, shown in Fig. 8a. The right side of Fig. 8a shows fine equiaxed $\alpha\text{-Fe}$ dendrites (dark) surrounded by $\text{Nd}_2\text{Fe}_{14}\text{B}$ (gray) and Nd-rich phases (bright), which is comparable with the microstructure in Fig. 6c. The high temperature above the melting point and a subsequent fast solidification rate of the melted material is the reason for the equiaxed morphology of these microstructural constituents. On the

opposite side in Fig. 8a, the plate-like morphology of the prior powder particles can be registered. At the contacts between the respective powder particles, the liquid phase is formed due to Joule heating, which joined the particles. This microstructure between the joined ribbons is comparable with the melted microstructure described before and consists of dark $\alpha\text{-Fe}$ dendrites, gray $\text{Nd}_2\text{Fe}_{14}\text{B}$, and bright Nd-rich phases.

The prior ribbons themselves consist of the gray $\text{Nd}_2\text{Fe}_{14}\text{B}$ phase in which bright Nd-rich phases are finely distributed. Using high discharge energies led to a dissociation of the metastable $\text{Nd}_2\text{Fe}_{14}\text{B}$ phase within the prior ribbon and therefore below the melting point, see Fig. 8b and c. The phase $\text{Nd}_2\text{Fe}_{14}\text{B}$ dissociated into finely dispersed bright precipitations due to an oxidation-driven dissociation reaction, as the Nd-oxides are thermodynamically stable. The

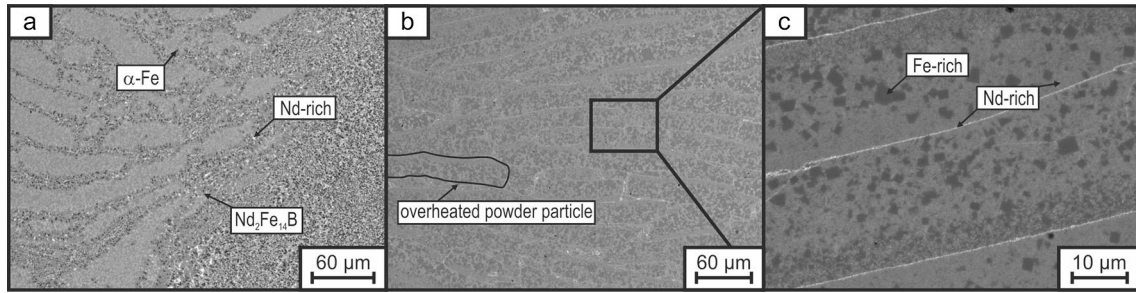


Fig. 8 EDS-densified specimen (50 kN/72 kJ): **a** transition zone of the fully densified and the melted zones of the EDS-densified NdFeB specimen; **b** and **c** overheated microstructure of the fully densified zone

oxygen content before and after the EDS process was measured and shows only a slight increase. Therefore, the oxygen for internal oxidation must have been already present inside the specimen or on the surfaces of the melt-spun powder in the initial state. Wuest et al. described a similar dissociation behavior of the $\text{Nd}_2\text{Fe}_{14}\text{B}$ phase into fine precipitations of Nd-rich and Fe-rich phases during spark plasma sintering [25].

High-resolution TEM micrographs of the initial powder and the fusion zone of two prior powder particles are shown in Fig. 9. The fusion zone of two prior powder particles is very narrow, see Fig. 9b. Despite the very short process time of the EDS method, grain coarsening has occurred comparing the grain size of Fig. 9a and c. As grain coarsening is caused not only by time but also by temperature, it can be assumed that very high temperatures close to the liquidus temperature occurred and grain coarsening in a short time is possible. Furthermore, the nanocrystalline microstructure of the initial powder is far away from equilibrium condition, which promotes a coarsening and thus minimization of the interfacial energy.

3.3 Magnetic properties

The influence of the process parameters (compression load and discharge energy) on the material density and the microstructure was discussed in the previous section. The degree of densification increases in the direction of higher discharge energies and compression loads. But in the microstructural section, it was discussed that an increase in discharge energy is accompanied by an increase of the area fraction of the melted zone as well as by an increase of dissociation reactions and grain coarsening of the nanocrystalline $\text{Nd}_2\text{Fe}_{14}\text{B}$ phase. These microstructural changes counteract the magnetic properties of the initial nanocrystalline NdFeB powder. Therefore, we want to discuss the magnetic properties regarding the microstructure formation during EDS processing and afterward, suitable process parameters for EDS densification of nanocrystalline NdFeB powder can be derived. The magnetic properties of the whole EDS-densified specimen for varying discharge energies E_{EDS} and compression loads p_{EDS} are shown in Fig. 10.

The volume fraction of the hard magnetic phase $\text{Nd}_2\text{Fe}_{14}\text{B}$ as well as the bulk density must be

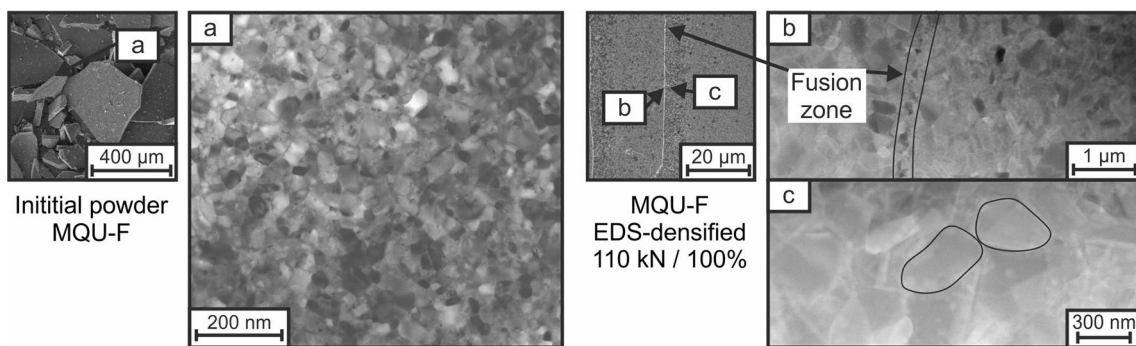


Fig. 9 TEM micrographs of **a** the initial powder MQU-F and **b** the fusion zone of two prior particles using high discharge energies 72 kJ

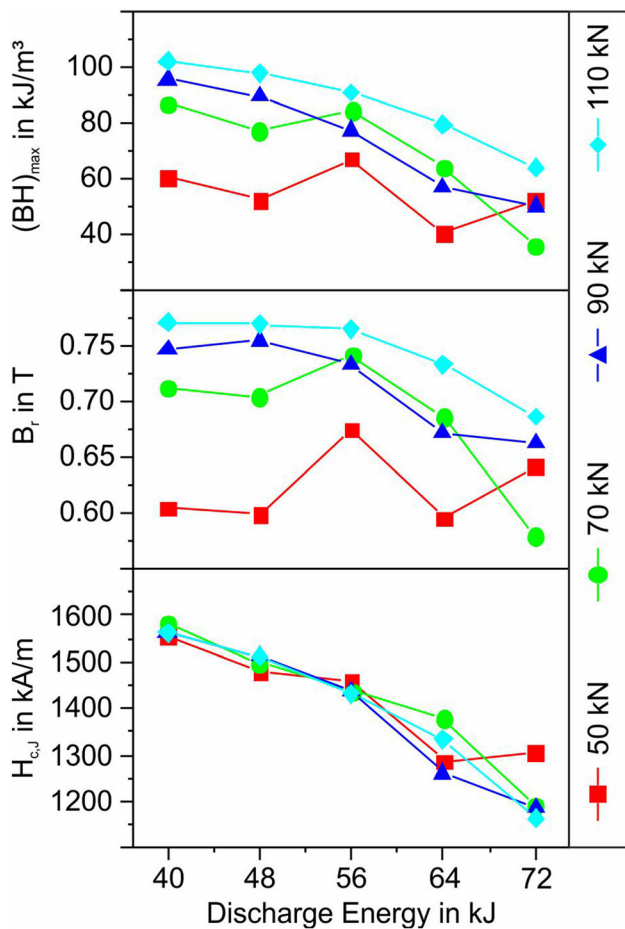


Fig. 10 Bulk magnetic properties with varying discharge energy E_{EDS} in kJ and compression load p_{EDS} in kN using 10 g of powder MQU-F [18]

maximized in the EDS-densified specimen to achieve a high remanence. Both the compression load p_{EDS} and the discharge energy E_{EDS} increase the bulk density, as discussed in the previous sections. An increase of the compression load p_{EDS} leads to higher densities without changing the microstructure significantly. An increase of the discharge energy E_{EDS} promotes the specimen's bulk density ρ as well, but the amount of liquid phase formed during EDS densification due to Joule heat is increased at the same time. The melting of the NdFeB powder during the EDS process leads to a dissociation of the nanocrystalline $\text{Nd}_2\text{Fe}_{14}\text{B}$ phase, which was set by the melt-spinning process. This liquid phase solidifies into a coarser microstructure that consists of α -Fe, $\text{Nd}_2\text{Fe}_{14}\text{B}$, $\text{Nd}_2\text{Fe}_{17}\text{B}_y$, and Nd-rich phases. Therefore, the local melting is accompanied by a reduction in the volume fraction of the nanocrystalline hard

magnetic phase $\text{Nd}_2\text{Fe}_{14}\text{B}$ which is accompanied by a lowering of the remanence. Additionally, using high discharge energies leads to an overheating of the former powder particles, as shown in Fig. 8b and c. Both the melting and the overheating increase the amount of α -Fe and Nd-rich phases (e.g., oxides) and lower, therefore, the magnetic properties [26, 27]. Increasing the discharge energy leads to lower coercivity values, as the amount of generated heat after Joule is higher. The generated heat in turn leads to melting, overheating, and grain coarsening of the nanocrystalline $\text{Nd}_2\text{Fe}_{14}\text{B}$ phase as discussed before and is associated with a decomposition of nanocrystalline hard magnetic phase. The compression load p_{EDS} only increases the density of the specimen and has less influence on the microstructure, so the compression load has no influence on the coercivity $H_{c,J}$.

In Fig. 11b, magnetic hysteresis of the whole specimen measured by a permagraph system is shown. It can be seen that the remanence and the coercivity decrease with increasing discharge energy and a constant compression load of 110 kN. This behavior was discussed in the previous section and is related to the microstructure that is formed during EDS.

VSM measurements on small samples cut from a bulk sample (EDS-densified with a compression load of 110 kN and discharge energy of 72 kJ) were performed to confirm that the magnetic properties of EDS-densified NdFeB magnets are locally different and strongly depends on the formed microstructure, see Fig. 11a. Compared to samples P1 and P2, samples P3 and P4 have low magnetic properties. SEM investigations, see Micrographs of Fig. 11, show that for sample P4, the amount of melted microstructure is higher than for sample P1, which is an explanation for the low magnetic properties. Sample P1 has a remanence B_r of nearly 0.8 T, but the coercivity $H_{c,J}$ is only in the range of 1200 kA/m , as a result of a high heat insertion due to Joule heating which is accompanied by the formation of a thin liquid seam and a grain coarsening of the nanocrystalline phase $\text{Nd}_2\text{Fe}_{14}\text{B}$.

For choosing the best possible EDS parameters for compaction of nanocrystalline NdFeB powder, the relationships listed below must be considered. The generated Joule heat and thus the discharge energy should be high enough to produce magnets with a high density. But too much heat will lead to a

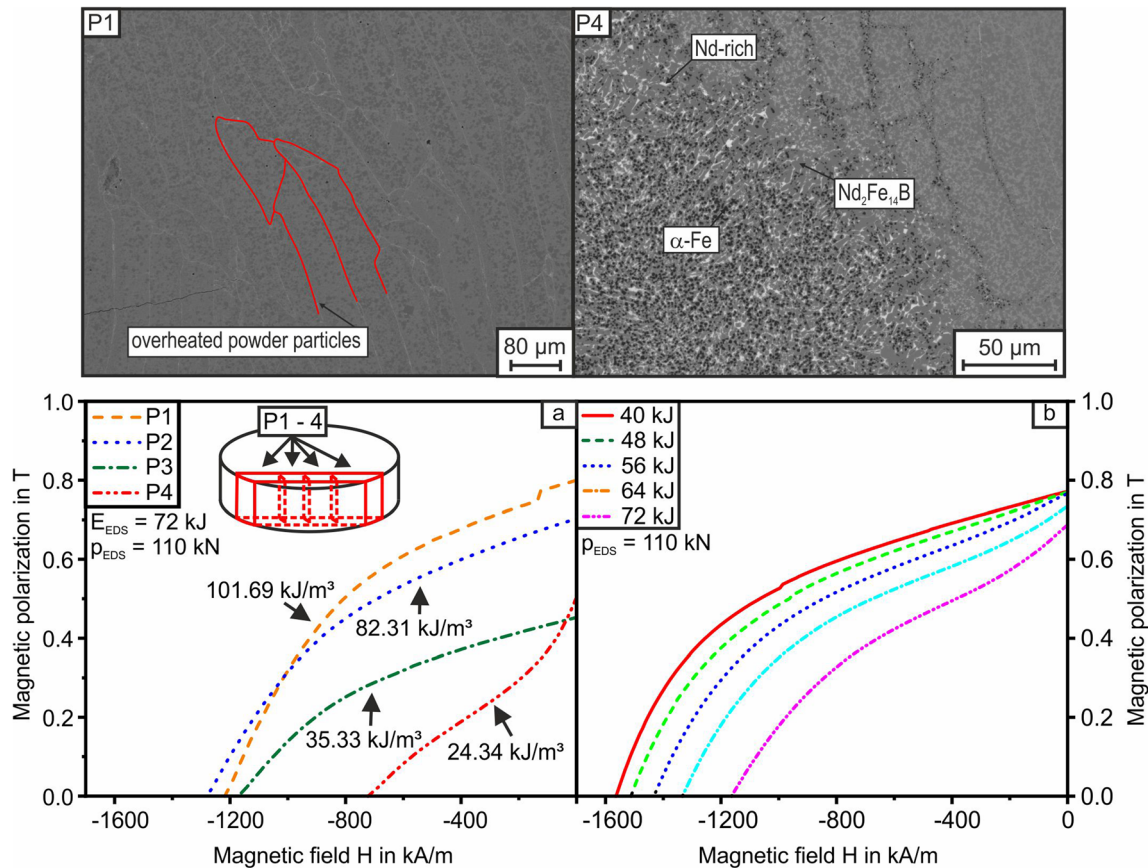


Fig. 11 Magnetic hystereses of EDS-densified NdFeB specimens: **a** local magnetic properties measured by VSM; **b** bulk magnetic properties measured by a permagraph system

dissociation of the hard magnetic phase $\text{Nd}_2\text{Fe}_{14}\text{B}$ and therefore a trade-off must be chosen. The applied load for the compaction of the powder loose can be as high as possible because the sample density will be increased without changing the microstructure of the initial powder, which would be associated with a decrease in the magnetic properties.

4 Conclusion

We have shown that it is possible to densify nanocrystalline NdFeB powder to achieve fully dense isotropic magnets with good magnetic properties using the electro-discharge sintering process. The key results are as follows:

1. The compression load determines the density of the pre-compacted powder loose and therefore influences the initial transition resistance before the capacitor discharge. The subsequent current

flow and generated Joule heat are influenced by the initial transition resistance.

2. The discharge energy determines the current flow and thus the generated Joule heat. The generated Joule heat promotes the formation of a liquid phase and thus the decomposition of the nanocrystalline hard magnetic phase $\text{Nd}_2\text{Fe}_{14}\text{B}$.
3. Reducing the volume fraction of the magnetic phase by applying to too high discharge energies will lead to a drop in the magnetic properties. Furthermore, using high discharge energies of 72 kJ and more leads to an overheating of the microstructure, resulting in dissolution reactions of the phase $\text{Nd}_2\text{Fe}_{14}\text{B}$ and grain coarsening and thus to a deterioration of the magnetic properties as well.
4. EDS-densified specimens have a microstructure that is characterized by three different zones – insufficiently densified, fully densified, and melted zones. The volume fraction of these three different zones that are formed during EDS

densification is affected by the used process parameters (compression load and discharge energy) and each zone has different magnetic properties.

- High compression loads of about 110 kN and moderate discharge energies of about 40 – 48 kJ lead to the highest magnetic properties and the optimal microstructure.

There are several reasons that this process can be transferred into applications in the future. The total energy consumption of the EDS process is low because the current is used directly (Joule Heat) for sintering and the process cycle (5 ms) is very short. Besides, it could be shown in another publication that magnetic scrap can be shredded at low cost and directly densified using EDS without process between. Furthermore, it is possible to integrate the EDS process into the hot pressing and hot flow process for the production of anisotropic NdFeB magnets. The integration is achieved by substituting the process steps of cold and hot pressing so that the EDS-compacted magnet only needs to be hot-extruded and anisotropic magnets could be produced. This would make an existing process for densifying anisotropic NdFeB more efficient.

Acknowledgement

We gratefully acknowledge financial support from the BMWi (Bundesministerium für Wirtschaft und Energie) within the project “Entwicklung eines Verfahrens zum Heißpressen von Magneten für energieeffiziente Pumpen (HeMag).”

Funding

Open Access funding enabled and organized by Projekt DEAL.

Open Access This article is licensed under a Creative Commons Attribution 4.0 International License, which permits use, sharing, adaptation, distribution and reproduction in any medium or format, as long as you give appropriate credit to the original author(s) and the source, provide a link to the Creative Commons licence, and indicate if changes were made. The images or other third party material in this article are included in the article’s Creative Commons

licence, unless indicated otherwise in a credit line to the material. If material is not included in the article’s Creative Commons licence and your intended use is not permitted by statutory regulation or exceeds the permitted use, you will need to obtain permission directly from the copyright holder. To view a copy of this licence, visit <http://creativecommons.org/licenses/by/4.0/>.

References

- J. J. Croat, Rapidly solidified neodymium-iron-boron permanent magnets (2017).
- D.P. Arnold, Review of microscale magnetic power generation. *IEEE Trans. Magn.* **43**(11), 3940–3951 (2007)
- J.F. Herbst, J.J. Croat, Neodymium-iron-boron permanent magnets. *J. Magn. Magn. Mater.* **100**(1–3), 57–78 (1991)
- D. Brown, B.-M. Ma, Z. Chen, Developments in the processing and properties of NdFeB-type permanent magnets. *J. Magn. Magn. Mater.* **248**(3), 432–440 (2002)
- S. Sugimoto, Current status and recent topics of rare-earth permanent magnets. *J. Phys. D* **44**(6), 64001 (2011)
- K.H.J. Buschow, F.R. Boer, *Physics of Magnetism and Magnetic Materials* (Kluwer Academic/Plenum Publishers, New York, 2003)
- M. Bram, A. Laptev, T. Prasad Mishra et al., Application of electric current assisted sintering techniques for the processing of advanced materials. *Adv. Eng. Mater.* (2020).
- E.A. Olevsky, D.V. Dudina, *Field-assisted sintering: science and applications* (Springer, Cham, 2018)
- S. Grasso, Y. Sakka, G. Maizza, Electric current activated/assisted sintering (ECAS): a review of patents 1906–2008. *Sci. Technol. Adv. Mater.* **10**(5), 53001 (2009)
- O. Guillon, J. Gonzalez-Julian, B. Dargatz et al., Field-assisted sintering technology/spark plasma sintering: mechanisms, materials, and technology developments. *Adv. Eng. Mater.* **16**(7), 830–849 (2014)
- M. Omori, Sintering, consolidation, reaction and crystal growth by the spark plasma system (SPS). *Mater. Sci. Eng. A* **287**(2), 183–188 (2000)
- P. Schütte, J. García, W. Theisen, Electro Discharge Sintering as a Process for Rapid Compaction in PM-Technology. Proceedings of the Euro International Powder Metallurgy Congress and Exhibition, Euro PM **3**, 2009 (2009)
- P. Schütte, H. Moll, and W. Theisen, “Electro Discharge Sintering—A new PM method to densify wear-resistant materials,” in 1st International Conference on Stone and Concrete Machining, pp. 171–176.

14. F.V. Lenel, Resistance sintering under pressure. *JOM* **7**(1), 158–167 (1955)
15. Z. Zhou, Y. Ma, J. Du et al., Fabrication and characterization of ultrafine grained tungsten by resistance sintering under ultra-high pressure. *Mater. Sci. Eng. A* **505**(1–2), 131–135 (2009)
16. M. Cologna, B. Rashkova, R. Raj, Flash sintering of nanograin zirconia in <5 s at 850°C. *J. Am. Ceram. Soc.* **93**(11), 3556–3559 (2010)
17. M. Yu, S. Grasso, R. Mckinnon et al., Review of flash sintering: materials, mechanisms and modeling. *Adv. Appl. Ceram.* **116**(1), 24–60 (2017)
18. L. Leich, A. Röttger, W. Theisen et al., Densification of nanocrystalline NdFeB magnets processed by electro-discharge sintering—microstructure, magnetic, and mechanical properties. *J. Magn. Magn. Mater.* **460**, 454–460 (2018)
19. L. Leich, A. Röttger, M. Krengel et al., Recycling of NdFeB magnets by electrodischarge sintering—microstructure, magnetic, and mechanical properties. *J. Sustain. Metall.* **5**(1), 107–117 (2019)
20. W. Schatt, B. Kieback, K.-P. Wieters (eds.), *Pulvermetallurgie: Technologien und Werkstoffe* (Springer, Berlin, 2007)
21. J. Gao, T. Volkman, S. Roth et al., Phase formation in undercooled NdFeB alloy droplets. *J. Magn. Magn. Mater.* **234**, 313–319 (2001)
22. J. Gao, T. Volkman, D.M. Herlach, A metastable phase crystallized from undercooled NdFeCoZrGaB alloy droplets. *J. Alloy. Compd.* **308**(1–2), 296–300 (2000)
23. J. Gao, B. Wei, Containerless solidification of undercooled NdFeZrB alloy droplets in a drop tube. *J. Alloy. Compd.* **285**(1–2), 229–232 (1999)
24. G. Schneider, E.-T. Henig, G. Petzow et al., Phase relations in the system Fe-Nd-B. *Mater. Res. Adv. Tech.* **77**, 775 (1986)
25. H. Wuest, L. Bommer, T. Weissgaerber et al., Magnetic and structural properties of spark plasma sintered nanocrystalline NdFeB-powders. *J. Magn. Magn. Mater.* **392**, 74–78 (2015)
26. W.C. Chang, T.S. Chin, K.S. Liu, The dissolution kinetics of free iron in Nd-Fe-B permanent magnet alloys. *J. Magn. Magn. Mater.* **80**(2–3), 352–358 (1989)
27. D.W. Scott, B.M. Ma, Y.L. Liang et al., Microstructural control of NdFeB cast ingots for achieving 50 MGOe sintered magnets. *J. Appl. Phys.* **79**(8), 4830 (1996)

Publisher's Note Springer Nature remains neutral with regard to jurisdictional claims in published maps and institutional affiliations.